An XFEM multiscale approach for fracture analysis of carbon nanotube reinforced concrete

CrossMark

Mehdi Eftekhari [a], Saeed Hatefi Ardakani [b], Soheil Mohammadi [b],*

[a] *Department of Civil Engineering, Rasht Branch, Islamic Azad University, Rasht, Iran*
[b] *High Performance Computing Lab, School of Civil Engineering, University of Tehran, Tehran, Iran*

A B S T R A C T

An XFEM multiscale approach is adopted in order to investigate the mechanical properties and fracture behavior of carbon nanotube reinforced concrete specimen. At the nanoscale, molecular dynamics simulation is used to find the mechanical properties of carbon nanotube (CNTs). Afterwards, a hydration model is adopted to find the chemical composition of cement paste. The hydrated model and CNTs are then converted into a finite element mesh for further analysis. Finally, at the meso scale the fracture behavior of the CNT reinforced concrete is simulated by the XFEM approach. The results indicate that the fracture energy of samples with similar volume fractions but reinforced by longer CNTs increase significantly, but addition of CNTs has little influence on the elastic modulus. In addition, the extent of crack propagation under a similar load level becomes considerably lower for the concrete samples reinforce by longer CNTs.

© 2014 Elsevier Ltd. All rights reserved.

1. Introduction

Concrete is the most common engineering material which is being used in the construction industry. Its composite action due to its constituent gradients, including coarse aggregates, sands and cement paste, has complicated its behavior, especially the fracture characteristics due to multiscale and multiphase natures of the material.

On the other hand, CNTs,[1] since their discovery in 1991 [1], have made a tremendous revolution in various industries due to their superior material properties, including high strength and low density. As a result, they are now being considered as an excellent alternative for conventional reinforcing fibers in the next generation of high-performance nanocomposites.

Using CNTs to reinforce concrete may result in the production of a high strength material [2–6]. Cwirzen et al. [2] indicated that addition of CNTs to the cement could increase the compressive strength up to 50%. Enhancing the fracture resistance properties, decreasing the porosity and shrinkage and long-term durability of the cementitious CNT-based material were other advantages of CNT additives [3]. Experimental results of Li et al. [4] illustrated that nanotubes could improve the flexural and compressive

strengths and failure strain of the cement matrix composite and decrease its porosity. Bridging across the crack and voids and enhancing the tensile load-transfer were also reported in their experiments.

The conventional practice of reinforcement of brittle materials to increase their strength and ductility can be implemented not only in the macroscale specimen, but also in the micro and nanoscales. CNTs can play the role of reinforcing components in several engineering materials. In recent years, several authors have used CNTs as the reinforcing component in the cement paste to enhance its mechanical properties. Among them, Hunashyal et al. [7] used an ultrasonic method in order to disperse MWCNTs[2] in the cement paste. Their results indicated that adding 0.5% of MWCNTs (by weigh) could increase the tensile strength and modulus by 19% and 70.9%, respectively. Mechanical properties of cement reinforced-CNTs were also investigated by Tyson et al. [8] using a three point bending test. Their results revealed the fact that adding 0.1% and 0.2% CNTs (by weight) to the cement matrix composites improved the strength, ductility, and fracture toughness. In another study, Musso et al. [9] found that adding 0.5% in weight of MWCNTs to plain cement paste enhanced the compressive stress approximately 34%. Šmilauer et al. [10] performed the experimental 3-point bending test on the CNT-based cement material. Their cement material contained CNT bundles with the diameter of 30 nm and the

---

length of 3 μm. The results showed that replacing 3.5% of the cement past with CHM[3] with grown CNT on its surface increased the fracture energy by 15%, from 16.5 N/m to 19 N/m.

Uniform distribution of CNT in the cement paste is practically very difficult, due to the fact that CNTs usually tend to agglomerate to each other. In order to obtain a more homogenous CNT-based material, a special treatment is necessary for the proper dispersion of the CNTs [10]. In recent year, several authors have proposed different effective methods for the dispersion of CNT in the cement material, among them, Sanchez and Ince [11] used silica fume and Konsta-Gdoutos et al. [3] employed surfactants for dispersing the CNT in the water. Another common approach is to functionalize the CNT with the carboxyl or hydroxyl groups attached to the surface of carbon atoms [3,6]. Alternatively, CNTs can be directly synthesized on the surface of cement grains, producing the cement hybrid material which can be easily blended with the conventional cement [6]. In this method, CNTs disperse uniformly in the cement volume.

The complex problem of cracking analysis of reinforced concrete structures has been a major challenge in the field of computational mechanics. Available numerical models for quasi-brittle fracture in the past decades have tried to provide a correct interpretation of energy dissipation in the fracture process zone. Among them, the smeared crack method [12–14], which relates the tangent of the softening curve to the size of the finite element and the fracture energy of material was adopted by Rabczuk et al. for 2-D fracture of reinforced concrete structures [15], and by Vecchio and DeRoo [16] for modeling of concrete tension splitting mechanisms. Alternatively, the powerful partition-of-unity enriched methods [17–24] have well developed in recent decade in the form of meshfree methods [17] or the extended finite element method [25].

The main focus of this multiscale study is to investigate the effects of adding CNTs on the mechanical and fracture properties of the cement-based materials, including concrete. To the best knowledge of the authors, no report is available on the multiscale fracture simulation of cement-based materials reinforced by CNTs. The paper begins with an overall discussion on adopted multiscale method in Section 2. Section 3 discusses the way the mechanical properties of CNTs at the nanoscale are determined using the MD[4] approach. In Section 4, the micromechanical properties of CNT-based cement paste are obtained, which is followed by presenting the approach for evaluation of the fracture behavior of CNT-reinforced concrete specimens at macroscales.

2. Multiscale approach

A sequential multiscale approach is adopted to study the fracture behavior of CNT-reinforced concrete specimens. Three scales are defined; the nano-scale for CNTs, the micro-scale for the CNT-reinforced cement and the meso-scale for XFEM[5] fracture analysis of concrete. At the nanoscale, the tensile behavior of CNTs is simulated by the molecular dynamics method. Then, the mechanical properties of the CNT are upscaled to the microscale. At the microscale, a hydration model is adopted in order to obtain chemical composition of the cement phase and then an RVE,[6] based on the results of the hydration method, is constructed and a finite element analysis (with the assumption of an isotropic damage model for all phases) is performed to capture the mechanical and damage properties of the CNT-reinforced cement paste. Afterwards, the homogenized response of the microscale is upscaled to an XFEM
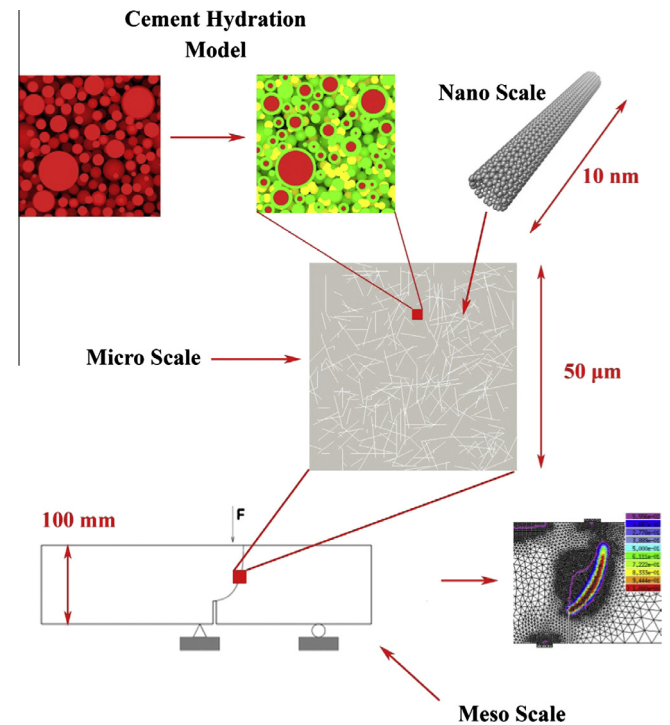

Fig. 1. Schematic representation of the multiscale simulation of CNT-reinforced cement.

damage analysis to predict the damage behavior of a three-bending test and a more general problem of the mixed mode crack propagation. The mentioned procedure is schematically depicted in Fig. 1.

3. Nanoscale

Several authors have recently studied the mechanical properties of CNTs. Fefey et al. [26] simulated SWCNTs[7] with vacancy defects by the MD approach and indicated that increasing the number of defects could decrease the elastic modulus. An atomistic-based progressive fracture model was used to study the fracture behavior of different CNTs using the finite element method by Tserpes and Papanikos [27] which led to the fact that the fracture stress and strain usually varied between 95–125 GPa and 15–20% Gpa, respectively. The mechanical properties of SWCNT and MWCNT with different length/diameter ratios under the tensile loading were investigated by Liew et al. [28]. The authors simulated single, double, triple and four-walled CNTs by MD and reported the tensile strength and elastic modulus varied between 132–168 GPa and 0.87–1.187 Tpa, respectively. Moreover, Jeng et al. [29] found that the mechanical properties of SWCNTs were significantly influenced by their chirality; i.e., the elastic modulus of 0.92–1.05 TPa, the failure stress around 132–168 GPa, and the Poisson's ratio of about 0.32–0.36. The buckling behavior of CNTs was also investigated by Eftekhari et al. [30]. They found that initial atomistic defects could largely reduce the buckling stress of CNTs but had little influence on their compressive elastic modulus. Despite the fact that such initial atomistic defects may influence the mechanical properties of CNTs, but their influence is out of the scope of the present study.

At the nanoscale, the LAMMPS[8] open source code [31], is employed to carry out the MD simulations of CNTs to capture their full-range stress–strain response, including potential fractures. The

---

[3] Cement hybrid material.
[4] Molecular dynamics.
[5] eXtended finite element method.
[6] Representative volume element.

[7] Single walled carbon nanotube.
[8] Large-scale atomic/molecular massively parallel simulator.

Table 1
Geometrical properties of CNTs.

Type	Diameter (Å)	Length/diameter
Armchair (10,10)	6.78	14.75
Zigzag (17,0)	6.65	15.04
Armchair (10,10)/(15,15)	10.17	9.83
Zigzag (17,0)/(26,0)	10.18	9.82

Table 2
Mechanical properties of the CNT.

Type	E (GPa)	v	F_t (GPa)	G_f (N/m)
Armchair (10,10)	1130	0.14	128.68	13,180,964
Zigzag (17,0)	1124	0.13	102.29	8,021,783
Armchair (10,10)/(15,15)	1087	0.14	125.84	12,264,589
Zigzag (17,0)/(26,0)	1068	0.13	99.88	7,732,911

Tersoff 3-body interatomic potential function [32] is employed to describe the repulsive/attractive interaction among the carbon atoms. In the Tersoff potential, the total potential energy of the system is described as:

$$E_{ij}^{Tersoff} = \frac{1}{2} f_C(r_{ij})[f_R(r_{ij}) + b_{ij} f_A(r_{ij})] \tag{1}$$

$$f_R(r_{ij}) = A_{ij} exp(-\lambda_{ij} r_{ij}), \quad f_A(r_{ij}) = -B_{ij} exp(-\mu_{ij} r_{ij}) \tag{2}$$

$$f_C(r_{ij}) = \begin{cases} 1, & r_{ij} \leqslant R_{ij} \\ \frac{1}{2} + \frac{1}{2} cos[\pi(r_{ij} - R_{ij})/(S_{ij} - R_{ij})], & R_{ij} < r_{ij} < S_{ij} \\ 0, & r_{ij} \geqslant S_{ij} \end{cases} \tag{3}$$

where r_{ij} is the interatomic distance between atoms i and j, functions $f_R(r_{ij})$ and $f_A(r_{ij})$ are the repulsive and attractive interactions, respectively, and $f_C(r_{ij})$ is the cut-off function. Further detail can be found in [32]. As Belytschko et al. mentioned in [33], using a rigid cut-off function may result in a more realistic stress–strain response when the CNT is subjected to the tensile loading. Therefore, instead of the smooth cut-off function in the original Tersoff potential [32], a rigid cut-off is used to prevent the non-physical increase in the tensile strength,

$$f_C(r_{ij}) = \begin{cases} 1 & r_{ij} < S_{ij} \\ 0 & r_{ij} \geqslant S_{ij} \end{cases} \tag{4}$$

CNTs may rarely bear compressive stresses in the coarser scales. As a result, only their tensile behavior is considered in this study. CNTs are produced in various forms. The structure of a CNT is defined by a chiral vector (n,m), where the case of $n = m$ represents
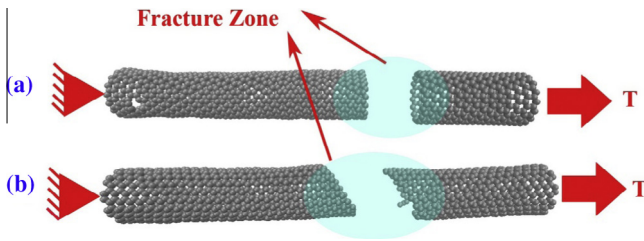

Fig. 4. Schematic hydration model in the cement paste.

Table 3
Particle size distribution of cement grain.

D (µm)	Cumulative volume distribution
6.59	0.000
8.36	0.395
9.74	0.449
11.35	0.506
13.22	0.566
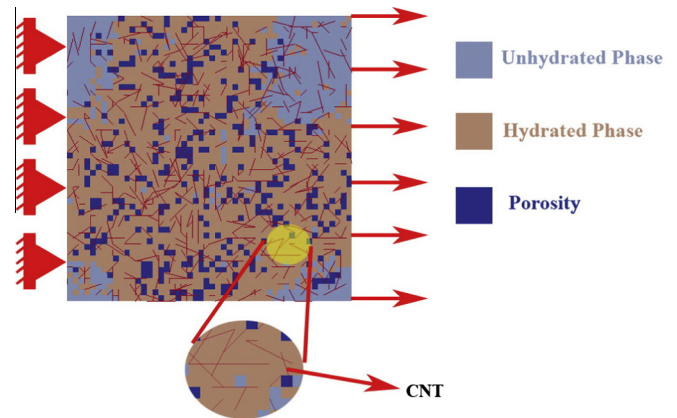
Fig. 5. Schematic mesh generation of the cement paste reinforced by CNTs.

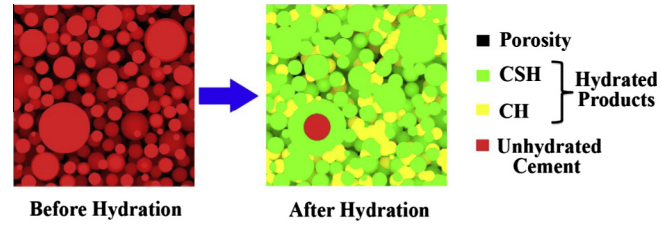**Fig. 2.** Different failure/fracture behaviors of CNTs under tension; (a) Zigzag CNT and (b) Armchair CNT.

Fig. 3. Stress–strain curve for the CNT under tension.

Table 4
Mechanical properties of the cement paste phases [10].

Phase	E (GPa)	v	F_t (MPa)	G_f (N/m)
Porosity	0.2	0.02	0.02	0.01
Unhydrated products	135	0.30	1800	118.5
Hydrated products	21.7	0.24	5.58	11.5

Table 5
Results of the verification model.

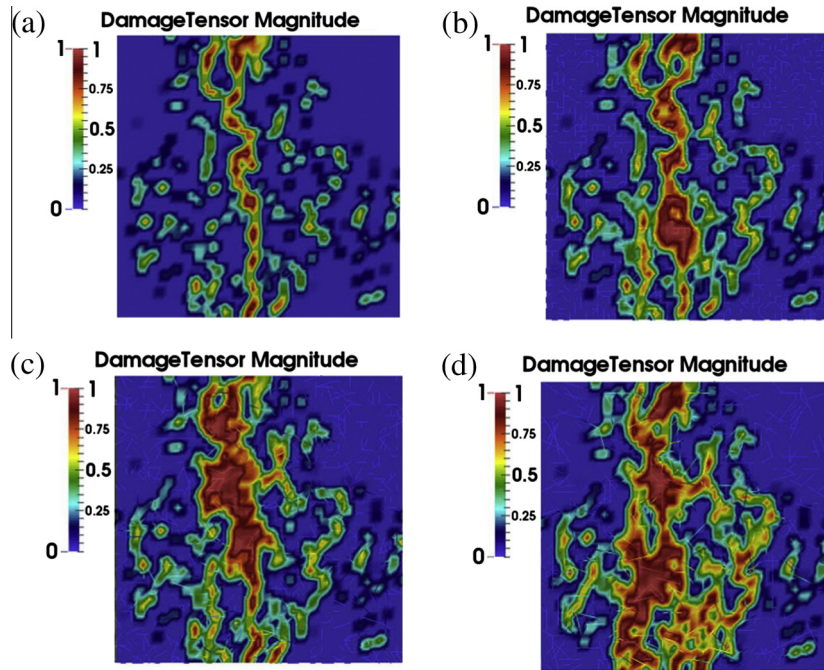|	Mechanical properties	Current study	Experimental [10]
Model-1	G (N/m)	21.7	20 (Mean value)
	f_t (Mpa)	3.21	–

Fig. 6. Damage distribution; (a) plane cement; (b) 1 μm CNT; (c) 3 μm CNT; and (d) 5 μm CNT.
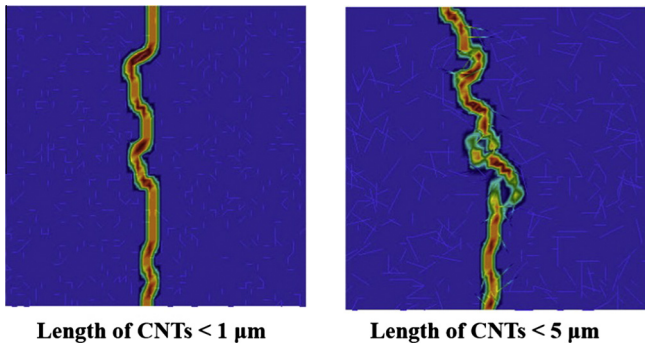

Fig. 7. Crack pattern in samples with different CNT length.

an Armchair CNT and $m = 0$ makes a Zigzag CNT. Due to the fact that the existing reports on experiments have not clearly stated the type of CNT, several types of CNTs may practically be used in construction of a CNT-based concrete specimen. Therefore, different failure responses are expected from a variety of CNTs, including MWCNTs and SWCNTs. Table 1 defines the geometrical specifications of various CNTs with lengths of 100 Å, which are considered for full stress–strain analysis to obtain the required mechanical and fracture properties. Afterwards, the mean value of their mechanical properties is considered for further analysis at the microscale.

At the first stage of simulation, the structure of CNT is relaxed to the room temperature (300 K) by adopting the NVT[9] ensemble in 20,000 steps. A random velocity is applied to all atoms in order to reach the desired temperature. The energy minimization procedure is then carried out by the CG[10] method to eliminate the residual stresses of CNT before the simulation.

After the system reaches the equilibrium state, simulations can be performed. The axial tension is applied at the one side of the
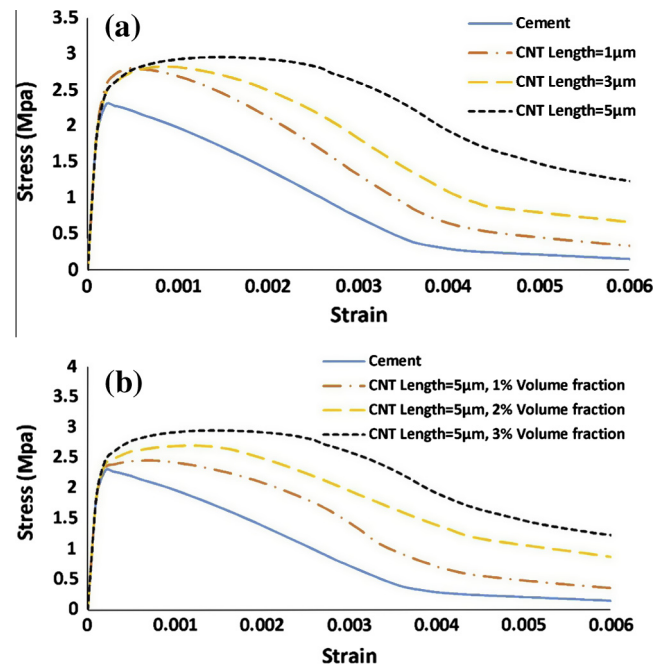

Fig. 8. Stress–strain curve for the cement and CNT-reinforce cement; (a) 3% CNT volume fraction and (b) CNT with the length of 5 μm.

CNT with the constant velocity of 0.01 Å/fs, while the atoms at the other side are restrained. The time integration step is set to 1 fs, and a total of 1,000,000 time steps are used to simulate the tensile behavior of CNTs. The axial stress of the CNT is defined by $\sigma = F/A$, where $A = \pi D t$, F is the axial force, D is the tube diameter, and t is the wall thickness. Several authors have recently adopted the interlayer spacing in graphite (0.34 nm) as the thickness of CNT [34–44], so this value is chosen for t.

Two different types of the failure/fracture behavior of the Zigzag (Fig. 2a) and Armchair CNTs (Fig. 2b) are illustrated in Fig. 2. The results of MD simulation indicate that for different CNTs, the

---

9 Constant Number of atoms, Volume and Temperature.
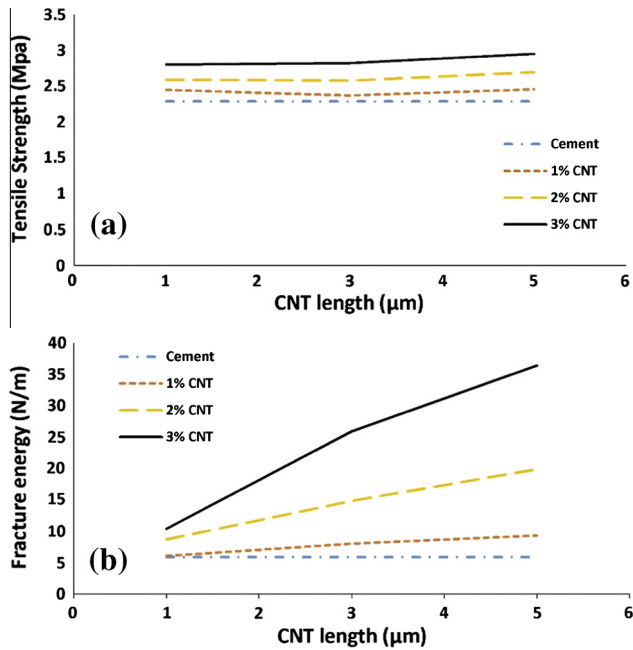10 Conjugate Gradient.

Fig. 9. (a) Tensile strength and (b) fracture energy of the CNT-reinforced cement.
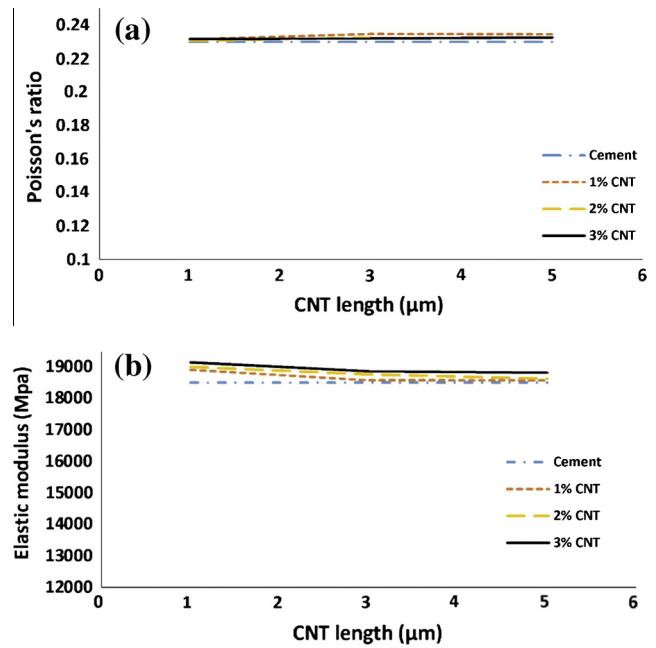

Fig. 10. (a) Poisson's ratio and (b) elastic modulus of the CNT-reinforced cement.

tensile stress and fracture energy actually depend on the chirality vector of the CNT, as depicted in Fig. 3. Clearly, the mechanical properties of Armchair CNTs are superior than the Zigzag one (Table 2), with significant differences for the fracture energy and tensile strength. However, the differences in Poisson's ratio and elastic modulus are practically negligible. The mean values of 1100 GPa, 114 GPa, and 1,030,000 N/m for the elastic modulus, the tensile strength and the fracture energy, respectively, are adopted for the microscale analysis.

4. Microscale

In order to obtain the mechanical properties of CNT-reinforced cement, the results of MD simulation are upscaled to the microlevel. Fracture energy, elastic modulus and the Poisson's ratio, obtained in the previous section, are used for the micromodel.

At the micro-scale, a micromechanical based finite element method is adopted in order to simulate the CNT-reinforced cement paste material. The cement itself is composed of three phases: the unhydrated phase, hydrated phase (calcium hydroxide and calcium silicate hydrate) and the capillary porosity [45], as depicted in Fig. 4.

Due to the fact that the major mechanical properties of the cement paste is the result of the chemical reaction of Alite or tricalcium silicate mineral ($3CaO \cdot SiO_2$ or C3S) and water in the Portland cement, which produces the CSH,[11] only the reaction of C3S is considered for the cement hydration in this study, as indeed accepted by others [45].

There are several cement hydration programs for developing the initial microstructure of the cement paste. The integrated Java-based particle kinetics model "μic" [46] is implemented for the hydration simulation. The cumulative volume distribution of cement grains with their diameters, determined from the PSD,[12] is presented in Table 3, where each value in the second column denotes the volume fraction of cement grain whose size is smaller than the value given in the first column.
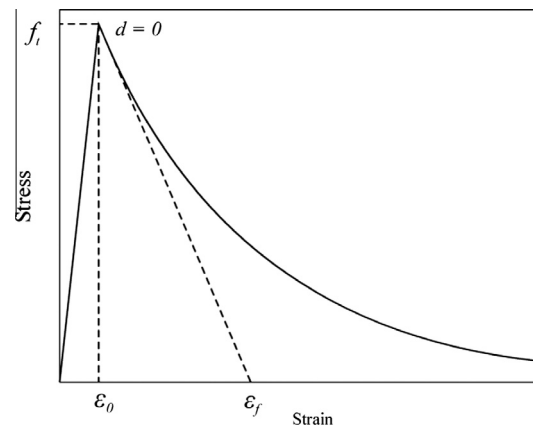

Fig. 11. Stress–strain curve with an exponential softening law.

The 3D microstructure of the hydrated cement paste at the microlevel is first generated and then a 2D slice of the 3D microstructure is mapped on a uniform mesh to perform the finite element simulation. During the hydration process, an RGB color is assigned to each pixel of the 2D hydration image. This RGB[13] color can be further used to assign the proper mechanical properties of each element in the generated mesh. Different types of modeling strategies have been proposed for simulating the CNTs. Wernik and Meguid [47] used a 3D space frame model for simulation of the CNT within a surrounding polymeric matrix. In addition, the CNT was modeled as a 3D solid element in the study conducted by Kulkarni et al. [48]. Alternatively, the single beam model which could sustain the bending force was implemented by Tserpes et al. [49] in simulation of CNT-reinforced composites. In order to simplify the finite element simulation of the cement, all the materials produced by the hydration simulation are put into 3 categories of the unhydrated phase (clinker), the hydrated phase (CSH) and the porosity (Fig. 5).

---

[11] Calcium Silicate Hydrate.
[12] Particle size distribution.
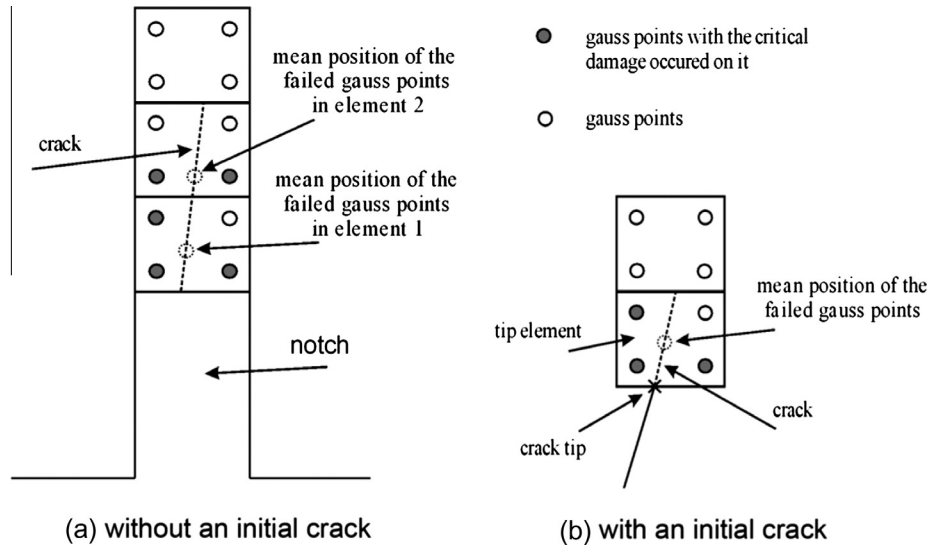
[13] Red-green-blue.

Fig. 12. Criteria for crack initiation and propagation based on damaged Gauss points.

Table 6
Material characteristics for different CNT volume fractions and lengths.

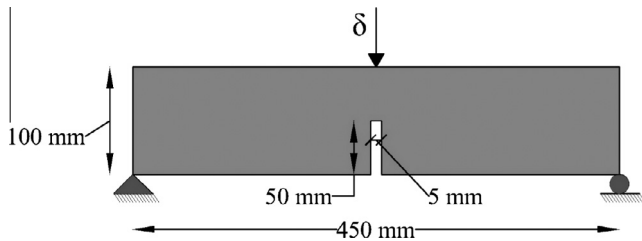| Material model	E (Gpa)	ν	F_t (Mpa)	G_f (N/m)
No.1 (plain paste)	18.50	0.23	2.29	5.89
No.2 (1%, L_{CNT} = 1 μm)	18.90	0.23	2.45	6.08
No.3 (1%, L_{CNT} = 3 μm)	18.60	0.23	2.37	8.07
No.4 (1%, L_{CNT} = 5 μm)	18.60	0.23	2.46	9.32
No.5 (3%, L_{CNT} = 1 μm)	19.14	0.23	2.80	10.4
No.6 (3%, L_{CNT} = 3 μm)	18.70	0.23	2.82	25.96
No.7 (3%, L_{CNT} = 5 μm)	18.80	0.23	2.95	36.43

Fig. 13. Three point bending beam; geometry and boundary conditions.

All the constituent materials which form the cement paste are considered as isotropic with the isotropic damage model, i.e. the stiffness modulus corresponding to each direction varies independent of the loading direction. The material degradation is implemented by an isotropic damage model with a linear softening law for all phases:

$$\sigma = (1 - \omega)E\varepsilon = f_t\left(1 - \frac{h\omega\varepsilon f_t}{2G_f}\right) \tag{5}$$

where σ is the stress, f_t is the uniaxial tensile strength, h is the effective width of the finite element, ε is the strain, G_f is the fracture energy, and ω is the damage parameter. The mechanical properties of the cement paste phases, taken from [10], are defined in Table 4. The mechanical properties of the porosity are limited to very small values to void convergence problems.

The size of the microstructure of the cement is 50×50 μm and the thickness is assumed to be 1 μm. The cross section of a bundle of CNT is assumed to be 0.05 μm². A combination of three CNT volume fractions (including 1%, 2% and 3%) and three lengths of CNTs (1 μm, 3 μm and 5 μm) provides nine models for analysis in this research. A random distribution based on the model of Matsumoto and Nishimura [50] is considered for both the orientation and the length of CNTs. A nonlinear plane stress simulation is performed in 1000 steps with the Newton–Raphson solver. The simulation is performed by the open source finite element package OOFEM [51]. The model is incrementally loaded by the applied strain and the corresponding stress is calculated.

The experimental results of Šmilauer et al. [10] are used to verify the results of the micromechanical simulation. A cement paste containing 3.47% volume fraction of the CNT with the length of 3 μm, which corresponds to the experimental results in [10], is considered. The results of the present numerical simulations are presented in Table 5, which show a good agreement with the experimental results.

Distribution of the damage on the surface of samples is illustrated in Fig. 6. Clearly, the damage propagation is increased in models which contain CNTs. The role of CNT length is also noticeable. When the length of CNT increases, larger amount of cement is integrated with CNTs and consequently more damaged areas are observed in samples with longer CNT (Fig. 6d) in comparison to the shorter one (Fig. 6b) As a result, more dissipated energy is predictable. The Paraview open source code was used for graphical representation.

Comparing the results of strain contours (Fig. 7) better illustrates that for a specific volume fraction of CNTs, when the length of CNTs increases, the potential failure path becomes longer, which results in more energy dissipation.

The models which are reinforced by CNT sustain more tensile stress with an increase in the ductility and fracture energy. The results of Fig. 8a indicate that for a specific volume fraction of CNTs, the sample which contains longer CNTs has more fracture energy. In addition, increasing the volume fraction of CNTs from 1% to 3% enhances the mechanical properties, including fracture energy and tensile strength (Fig. 8b). It should be noted that, despite the fact that adding more CNTs can enhance the mechanical properties, no experimental tests have reported the use of more than 3% volume fraction of CNTs. Therefore, only simulation of samples with less than 3% CNT volume fraction is considered in this study.

Increasing the length and volume fraction of CNTs can lead to an increase in the tensile strength and fracture energy. The length
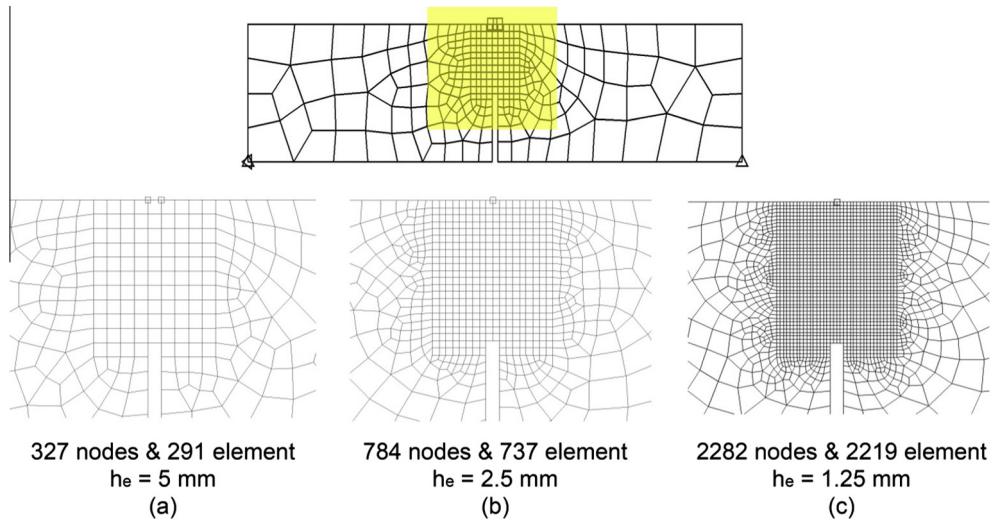
327 nodes & 291 element
h_e = 5 mm
(a)

784 nodes & 737 element
h_e = 2.5 mm
(b)

2282 nodes & 2219 element
h_e = 1.25 mm
(c)

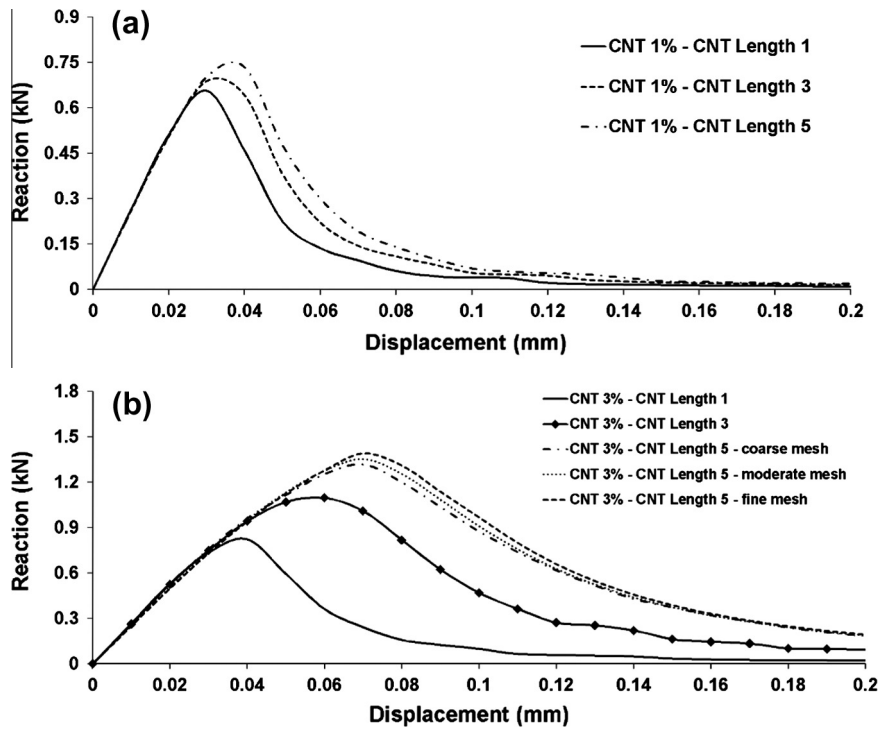**Fig. 14.** Three finite element meshes for simulation of the bending beam.

Fig. 15. Force–displacement curves for different CNT volume fractions and CNT lengths; (a) 1% CNT volume fraction and (b) 3% CNT volume fraction.

of CNTs also plays a significant role, i.e., for a constant volume fraction of CNTs, longer CNTs are more effective than the shorter ones (Fig. 9), where a maximum value of 2.95 MPa tensile strength and 36.43 N/m fracture energy are predicted for the sample which contains 5 μm CNTs.

Due to the fact that the CNT-reinforced cement is assumed isotropic, the Poisson's ratio of each sample can be obtained by calculating the negative ratio of transverse to axial strain, as illustrated in Fig. 10a. It is clear that increasing the volume fraction of the CNT leads to a slight increase in the Poisson's ratio, which is practically negligible and a mean value of 0.23 for the CNT-reinforced cement can be adopted. In comparison with the CNT volume fraction, the CNT length does not significantly affect the Poisson's ratio. While, the elastic modulus is not so susceptible to the length of the

CNT, its volume fraction plays a significant role. Fig. 10b illustrates variations of elastic modulus for different values of CNT volume fractions. By increasing the volume fraction of the CNT, the elastic modulus increases, but the length of CNTs does not affect the Young's modulus.

5. Meso scale

The results of microscale simulation are upscaled to the meso scale solutions, as schematically shown in Fig. 1. These include E, v, f_t and G_f for the plain paste and the CNT reinforced paste. They are employed for damage analysis and crack propagation at the meso scale. First, an elastic-damage analysis is performed. A crack can then be introduced after the criterion for crack initiation is sat-

isfied. A full XFEM crack propagation analysis will then be performed.

5.1. XFEM and the continuum damage model

The well-developed extended finite element method [52,53] is adopted for crack analysis at the meso scale. Based on the general definition of XFEM approximation, the displacement field for a point x can be approximated by:

$$\boldsymbol{u}(x) = \sum_i N_i(x)u_i + \sum_j N_j(x)\psi_j(x)a_j \tag{6}$$

where u is the nodal displacement, a is the enriched degrees of freedom, N is the finite element shape function and ψ is the enrichment function.

Due to the fact that a damage analysis is performed, only the discontinuity of the crack should be considered, and the crack-tip singularity is practically avoided. As a result, approximation (6) is explicitly defined in terms of the discontinuity enrichment by the Heaviside function $H(x)$,

$$\psi_j(x) = H(x) = \begin{cases} +1 & \text{if } (x - x^*) \cdot n \geqslant 0 \\ -1 & \text{otherwise} \end{cases} \tag{7}$$

where x^* is the nearest point to the point x on Γ_c and n is the normal vector to Γ_c at the point x^*. By introducing $\xi = (x - x^*) \cdot n$, the XFEM approximation (6) can be written as,

$$u(x) = \sum_{i=1}^n N_i(x)u_i + \sum_{k=1}^m N_k(x)(H(\xi) - H(\xi_k))a_k \tag{8}$$

Moreover, the constitutive damage model can be defined as,

$$\boldsymbol{\sigma} = (1 - d)\bar{\boldsymbol{\sigma}} = (1 - d)\boldsymbol{C} : \boldsymbol{\varepsilon} \tag{9}$$

where $\boldsymbol{\sigma}$ is the Cauchy stress tensor, $\boldsymbol{\varepsilon}$ is the strain tensor, $\bar{\boldsymbol{\sigma}}$ is the effective tensor, $\boldsymbol{C}$ is the isotropic linear-elastic stiffness tensor and d is the damage parameter which ranges between 0 (the intact material) and 1 (the fully damaged material). The loading–unloading condition in terms of the damage loading function f is defined as:

$$f(\boldsymbol{\varepsilon}, \tau) = \varepsilon_{eq}(\boldsymbol{\varepsilon}) - \tau \leqslant 0, \quad \dot{\tau} \geqslant 0, \quad f(\boldsymbol{\varepsilon}, \tau)\dot{\tau} = 0 \tag{10}$$
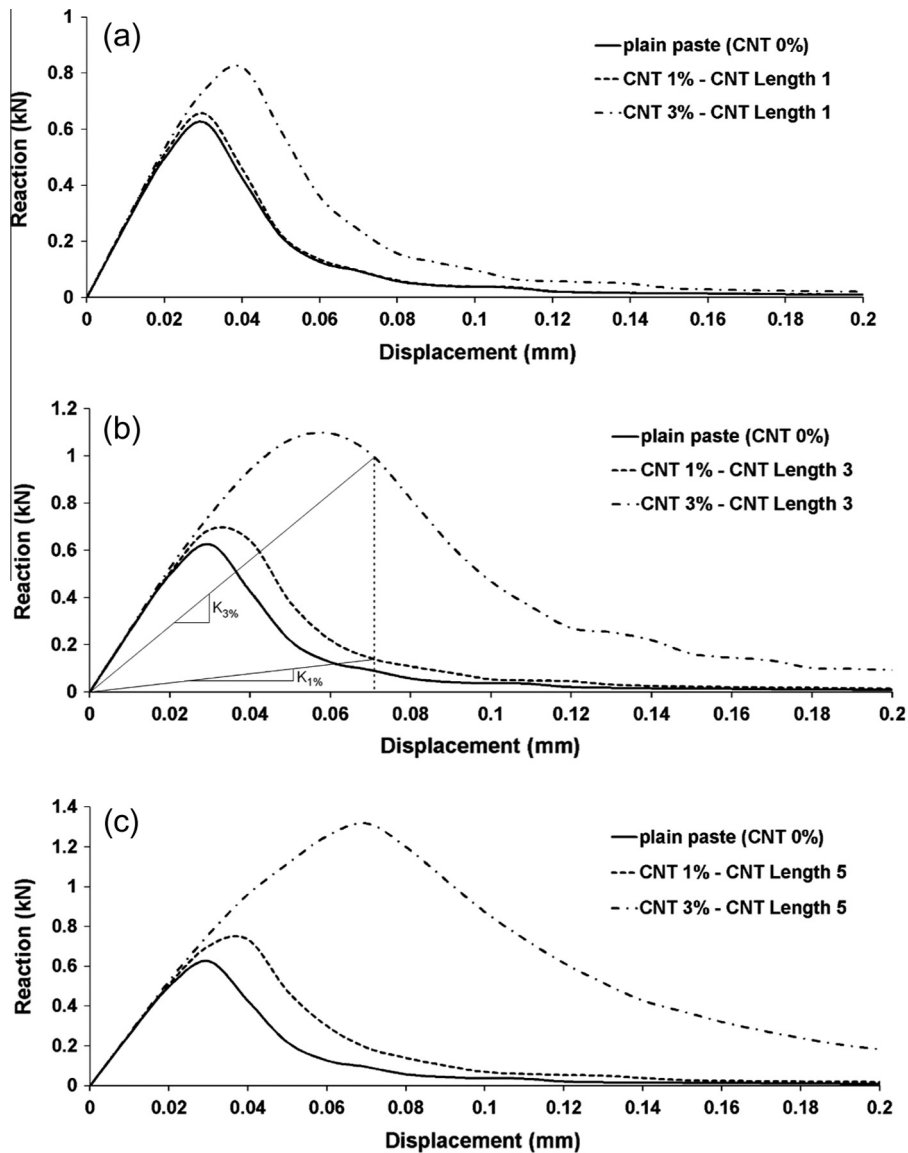

Fig. 16. Force–displacement curves for different CNT lengths and different volume fractions; (a) 1 μm CNT; (b) 3 μm CNT; (c) 5 μm CNT.
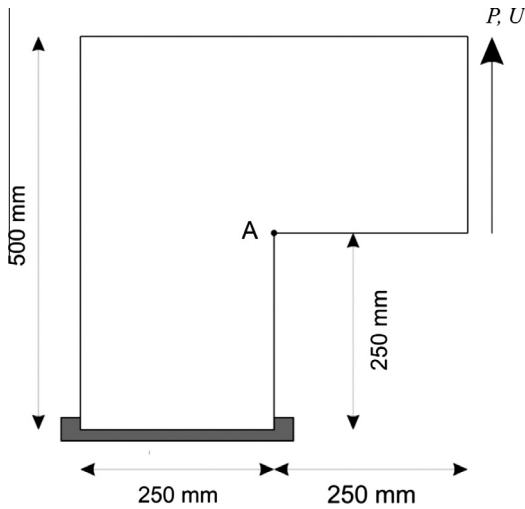
Fig. 17. L-shaped frame test; geometry and boundary conditions.

where $H_{dis} = \frac{f_t^2 l_c}{2 G_F E - f_t^2 l_c}$ is the softening parameter, G_F is the fracture energy of material and l_c is a characteristic length which represents the width of the damage concentration. In general, l_c depends on the size, shape and direction of the elements in numerical analysis. Based on the results of [13], two values of $l_c = \sqrt{A}$ and $l_c = \sqrt{2A}$ are assumed for the crack band width, depending on the alignment and non-alignment of the damage band and finite elements, respectively. The numerical results have shown that these assumptions may well eliminate or substantially reduce the mesh dependency of the results.

In order to implement an accurate approach to transform the damage region into a macroscopic crack, a simple technique based on checking the damage parameter in each integration point ahead of discontinuity against a critical damage (d_{cr} = 0.99) is adopted. A traction free discontinuity in that element will then be formed by the XFEM technique.

According to Fig. 12, two potential crack propagation states may occur. In the first case, an initial crack does not exist and the objective is to form the initial crack path. In this case, once two elements have experienced the critical damage, the line which connects the mean positions of the damaged integration points (from the first element to the second one) forms the crack path (see Fig. 12a). In the second case, the domain does include an initial crack, and the objective is to predict the crack propagation path. Here, the crack is further extended from the existing crack tip towards the mean position of the integration points which have violated the critical damage d_{cr} (see Fig. 12b).

5.2. Numerical simulations

Two examples are presented to demonstrate the final meso scale solutions based on previously-discussed nano and microscale simulations. The first example is a mode-I three point bending test, for which the effects of different CNT volume fractions and lengths on the global response of the problem are examined. In the second example, a mixed mode problem is studied and the effect of inclusion of two different CNT lengths on crack propagation is investigated. Seven types of material properties, obtained from the numerical micro-level simulations, are considered (see Table 6). The first model is related to the plain paste, while the others represent different CNT reinforcement compositions.

5.2.1. Three point bending beam

A centrally notched three-point bending beam, composed of CNT-reinforced cement, is simulated by the extended finite element method to estimate the load–displacement behavior of the specimen for different volumetric fractions and lengths of CNTs.
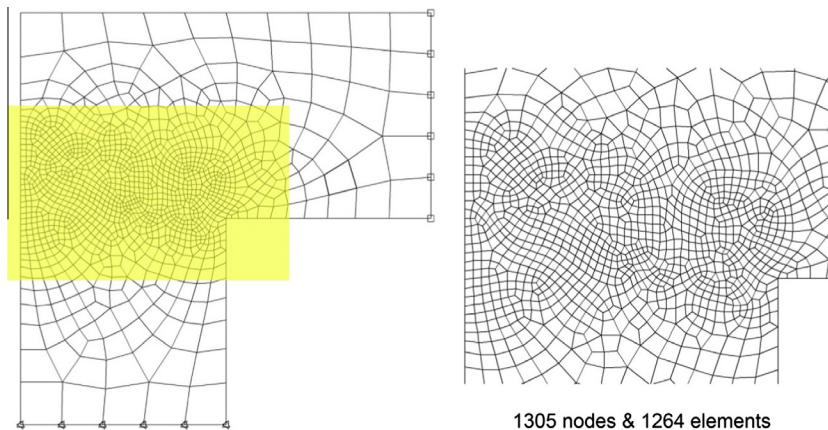
where ε_{eq} is the equivalent strain variable, τ is the maximum of equivalent strain that the material has experienced so far. The internal variable τ controls the level of damage growth. The Rankine equivalent strain is used to define the equivalent strain ε_{eq} [54],

$$\varepsilon_{eq}(\boldsymbol{\varepsilon}) = \frac{1}{E} \max_{I=1,2,3} \bar{\sigma}_I(\boldsymbol{\varepsilon}) \tag{11}$$

where E is the Young's module and $\bar{\sigma}_I$ is the principal effective stress. Here, an exponential softening damage law is adopted [54,55] (Fig. 11),

$$d = g(\tau) \equiv \begin{cases} 0 & \text{for } \tau \leqslant \varepsilon_0 \\ 1 - \frac{\varepsilon_0}{\tau} \exp\left(-\frac{\tau - \varepsilon_0}{\varepsilon_f - \varepsilon_0}\right) & \text{for } \tau > \varepsilon_0 \end{cases} \tag{12}$$

where ε_0 is the maximum elastic strain and parameter ε_f controls the slope of the softening curve.

The softening behavior of the material leads to generation of inelastic strains and damage in a thin band which may subsequently result in mesh dependency of the numerical solution. The crack band method [12–14] is adopted to overcome this problem. Accordingly, the final form of the damage law can be written as [54]:

$$d = g(\tau) \equiv \begin{cases} 0 & \text{for } \tau \leqslant \varepsilon_0 \\ 1 - \frac{\varepsilon_0}{\tau} \exp\left(-\frac{\tau - \varepsilon_0}{\varepsilon_0} \times 2 H_{dis}\right) & \text{for } \tau > \varepsilon_0 \end{cases} \tag{13}$$

1305 nodes & 1264 elements

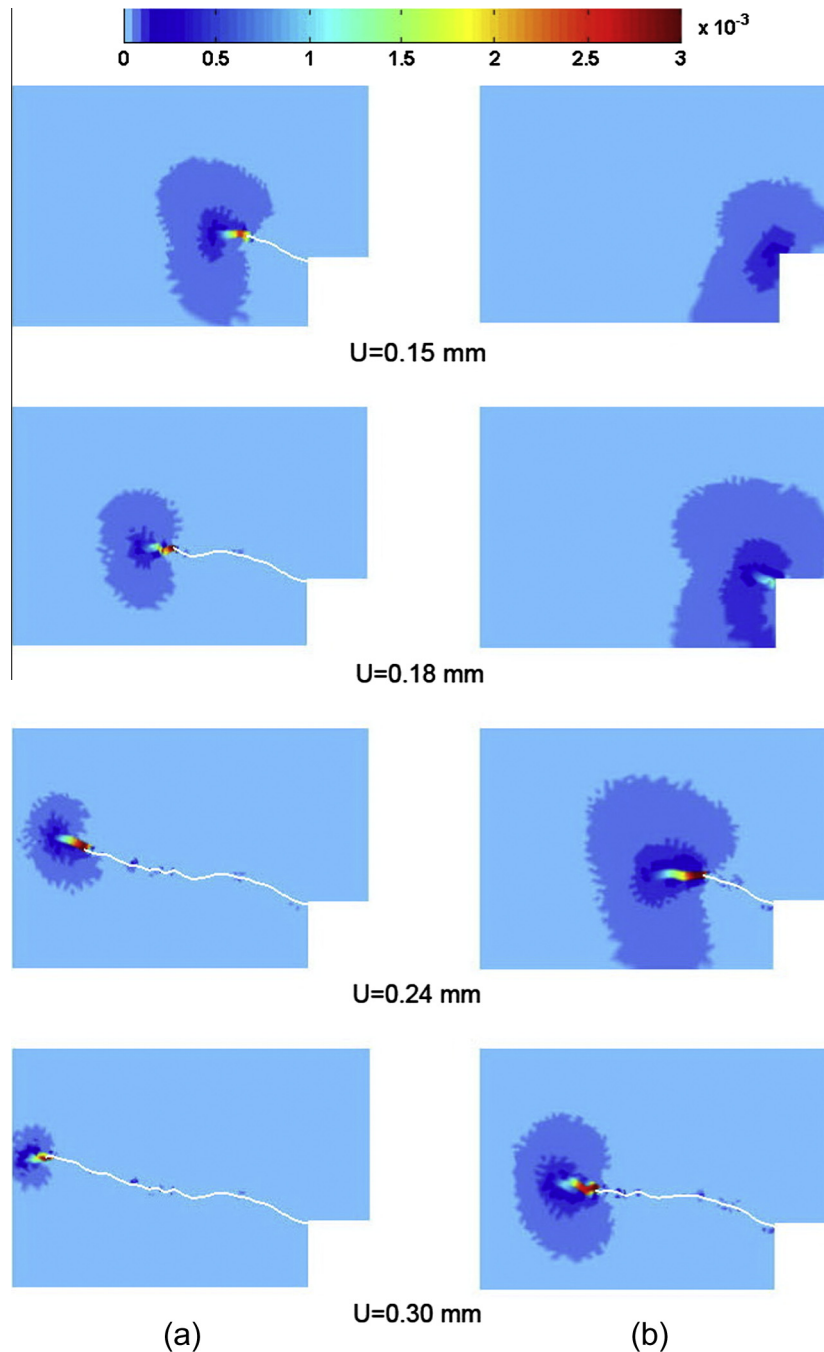**Fig. 18.** The finite element mesh.

Fig. 19. Equivalent strain (ε_{eq}) contours at different stretches for (a) 3% CNT with length of 1 μm and (b) 3% CNT with length of 5 μm.

The dimensions and boundary conditions of this problem are depicted in Fig. 13.

The thickness of the beam is 100 mm and the problem is analyzed in the plane strain state. The beam is loaded up to $\delta = 0.2$ mm and the damage extension virtually represents a mode-I fracture problem.

Three types of finite element meshes with bilinear quadrilateral elements are used to discretize the domain, as shown in Fig. 14. For each case, the average mesh-size in the zone affected by the tensile damage (h_e) is specified.

The effect of CNT length on the force–displacement curve for two CNT volume fractions (1% and 3%) are depicted in Fig. 15. Clearly, while for the low volume fraction of 1% (Fig. 15a), the length of CNT has a limited effect on the global response of the

beam, a significant effect is observed for the 3% CNT volume fraction (Fig. 15b).

Moreover, Fig. 15b compares the results for different meshes which shows the insensitivity of the solution to the FEM[14] mesh sizes. In fact, the potential mesh dependency of the softening part of force–displacement curve is well avoided by the crack band model.

In addition, Fig. 16 shows the effect of different CNT volume fractions on the global response of the beam for each of three CNT lengths (1 μm, 3 μm, 5 μm). Expectedly, for a constant CNT length, the increase in CNT volume fraction significantly increases both P_u and K ($K_{3\%} > K_{1\%}$ in Fig. 16b); showing almost 100% increase
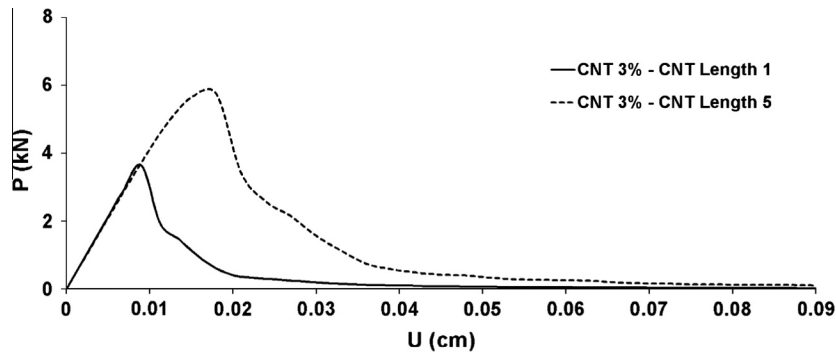
---

[14] Finite element Method.

Fig. 20. Force–displacement curve for the 3% CNT volume fraction and two CNT lengths.

in the ultimate load bearing by addition of 3% of 5 μm CNTs into the plain cement.

5.2.2. L-shaped frame test

An L-shaped frame test, composed of CNT-reinforced cement, is simulated by the extended finite element method to predict the effect of two different CNT lengths (1 μm and 5 μm) on load bearing capacity and mixed mode crack propagation. Dimensions and boundary conditions of this problem are depicted in Fig. 17.

The thickness of the beam is 100 mm and the problem is analyzed in the plane strain state and the frame is loaded up to $U = 0.9$ mm. Due to stress concentration at the point A in Fig. 17, the crack initiates and propagates in a mixed mode state. A finite element mesh with bilinear quadrilateral elements is used to discretize the domain, as shown in Fig. 18.

Evolution of the fracture process zone along with the propagation of traction-free discontinuity is demonstrated in Fig. 19 for the case of 3% CNTs with lengths of 1 μm and 5 μm. Despite the fact the final crack path remains almost the same for the two cases, a remarkable delay in crack propagation is observed for the case of longer CNTs (with similar volume fraction). The reason for this delay can be justified by considering the force–displacement curve presented in Fig. 20, which shows that when the length of CNTs is 5 μm, the maximum resistance and the fracture energy increase substantially, leading to a long delay in crack propagation in comparison with the low-length CNTs. In both cases, during the process of crack propagation, the contours of equivalent strain ε_{eq} (Fig. 19) show the unloaded banded region around crack faces in front of the crack tip.

6. Conclusion

In this research an XFEM-multiscale approach is adopted to investigate the mechanical properties and fracture behavior of carbon nanotube (CNT)-reinforced concrete. The results of microsimulation indicate that the fracture energy of the cement reinforced by longer CNTs significantly increase, but addition of CNTs has little influence on the elastic modulus. In addition, much longer crack propagation paths should be generated prior to the final tensile failure.

In the meso scale, the extended finite element method is applied for modeling crack propagation in CNT-reinforced cement using the elastic-damage model. It can be observed, for a constant CNT length, that the increase in CNT volume fraction significantly increases both P_u and K. Also a remarkable delay in mixed mode crack initiation and propagation is observed for the case of longer CNTs.

References

[1] S. Iijima, Helical microtubules of graphitic carbon, Nature 354 (1991) 56–58.
[2] A. Cwirzen, K. Habermehl-Cwirzen, V. Penttala, Surface decoration of carbon nanotubes and mechanical properties of cement/carbon nanotube composites, in: Advances in Cement Research, 2008, pp. 65–73.
[3] M.S. Konsta-Gdoutos, Z.S. Metaxa, S.P. Shah, Multi-scale mechanical and fracture characteristics and early-age strain capacity of high performance carbon nanotube/cement nanocomposites, Cem. Concr. Compos. 32 (2010) 110–115.
[4] G.Y. Li, P.M. Wang, X. Zhao, Mechanical behavior and microstructure of cement composites incorporating surface-treated multi-walled carbon nanotubes, Carbon 43 (2005) 1239–1245.
[5] Z. Metaxa, M. Konsta-Gdoutos, S. Shah, Mechanical properties and nanostructure of cement-based materials reinforced with carbon nanofibers and polyvinyl alcohol (PVA) microfibers, ACI Spec. Publ. 270 (2010).
[6] A.G. Nasibulin, S.D. Shandakov, L.I. Nasibulina, A. Cwirzen, P.R. Mudimela, K. Habermehl-Cwirzen, D.A. Grishin, Y.V. Gavrilov, J.E.M. Malm, U. Tapper, Y. Tian, V. Penttala, M.J. Karppinen, E.I. Kauppinen, A novel cement-based hybrid material, New J. Phys. 11 (2009) 023013.
[7] A.M. Hunashyal, S.V. Tippa, S.S. Quadri, N.R. Banapurmath, Experimental investigation on effect of carbon nanotubes and carbon fibres on the behavior of plain cement mortar composite round bars under direct tension, ISRN Nanotechnol. 2011 (2011) 6.
[8] R. Abu Al-Rub, B. Tyson, A. Yazdanbakhsh, Z. Grasley, Mechanical properties of nanocomposite cement incorporating surface-treated and untreated carbon nanotubes and carbon nanofibers, J. Nanomech. Micromech. 2 (2012) 1–6.
[9] S. Musso, J.-M. Tulliani, G. Ferro, A. Tagliaferro, Influence of carbon nanotubes structure on the mechanical behavior of cement composites, Compos. Sci. Technol. 69 (2009) 1985–1990.
[10] V. Šmilauer, P. Hlaváček, P. Padevět, Micromechanical analysis of cement paste with carbon nanotubes, Acta Polytech. 52 (2012) 22–28.
[11] F. Sanchez, C. Ince, Microstructure and macroscopic properties of hybrid carbon nanofiber/silica fume cement composites, Compos. Sci. Technol. 69 (2009) 1310–1318.
[12] Z. Bažant, B.H. Oh, Crack band theory for fracture of concrete, Mater. Constr. 16 (1983) 155–177.
[13] J. Rots, Computational modeling of concrete fracture, in: Civ. Eng. Geosci., Delft University of Technology, 1988.
[14] J. Oliver, A consistent characteristic length for smeared cracking models, Int. J. Numer. Methods Eng. 28 (1989) 461–474.
[15] T. Rabczuk, J. Akkermann, J. Eibl, A numerical model for reinforced concrete structures, Int. J. Solids Struct. 42 (2005) 1327–1354.
[16] F. Vecchio, A. DeRoo, Smeared-crack modeling of concrete tension splitting, J. Eng. Mech. 121 (1995) 702–708.
[17] T. Rabczuk, T. Belytschko, Cracking particles: a simplified meshfree method for arbitrary evolving cracks, Int. J. Numer. Methods Eng. 61 (2004) 2316–2343.
[18] T. Rabczuk, T. Belytschko, Application of particle methods to static fracture of reinforced concrete structures, Int. J. Fract. 137 (2006) 19–49.

[19] T. Rabczuk, T. Belytschko, A three-dimensional large deformation meshfree method for arbitrary evolving cracks, Comput. Methods Appl. Mech. Eng. 196 (2007) 2777–2799.

[20] T. Rabczuk, J. Eibl, Numerical analysis of prestressed concrete beams using a coupled element free Galerkin/finite element approach, Int. J. Solids Struct. 41 (2004) 1061–1080.

[21] T. Rabczuk, J. Eibl, L. Stempniewski, Numerical analysis of high speed concrete fragmentation using a meshfree Lagrangian method, Eng. Fract. Mech. 71 (2004) 547–556.

[22] T. Rabczuk, G. Zi, S. Bordas, H. Nguyen-Xuan, A geometrically non-linear three-dimensional cohesive crack method for reinforced concrete structures, Eng. Fract. Mech. 75 (2008) 4740–4758.

[23] T. Rabczuk, G. Zi, S. Bordas, H. Nguyen-Xuan, A simple and robust three-dimensional cracking-particle method without enrichment, Comput. Methods Appl. Mech. Eng. 199 (2010) 2437–2455.

[24] X. Zhuang, C.E. Augarde, K.M. Mathisen, Fracture modeling using meshless methods and level sets in 3D: framework and modeling, Int. J. Numer. Methods Eng. 92 (2012) 969–998.

[25] J.F. Unger, S. Eckardt, C. Könke, Modelling of cohesive crack growth in concrete structures with the extended finite element method, Comput. Methods Appl. Mech. Eng. 196 (2007) 4087–4100.

[26] E.G. Fefey, R. Mohan, A. Kelkar, Computational study of the effect of carbon vacancy defects on the Young's modulus of (6, 6) single wall carbon nanotube, Mater. Sci. Eng.: B 176 (2011) 693–700.

[27] K.I. Tserpes, P. Papanikos, The effect of Stone–Wales defect on the tensile behavior and fracture of single-walled carbon nanotubes, Compos. Struct. 79 (2007) 581–589.

[28] K.M. Liew, X.Q. He, C.H. Wong, On the study of elastic and plastic properties of multi-walled carbon nanotubes under axial tension using molecular dynamics simulation, Acta Mater. 52 (2004) 2521–2527.

[29] Y.-R. Jeng, P.-C. Tsai, T.-H. Fang, Effects of temperature and vacancy defects on tensile deformation of single-walled carbon nanotubes, J. Phys. Chem. Solids 65 (2004) 1849–1856.

[30] M. Eftekhari, S. Mohammadi, A.R. Khoei, Effect of defects on the local shell buckling and post-buckling behavior of single and multi-walled carbon nanotubes, Comput. Mater. Sci. 79 (2013) 736–744.

[31] S. Plimpton, Fast parallel algorithms for short-range molecular dynamics, J. Comput. Phys. 117 (1995) 1–19.

[32] J. Tersoff, Modeling solid-state chemistry: interatomic potentials for multicomponent systems, Phys. Rev. B 39 (1989) 5566–5568.

[33] T. Belytschko, S.P. Xiao, G.C. Schatz, R.S. Ruoff, Atomistic simulations of nanotube fracture, Phys. Rev. B 65 (2002) 235430.

[34] S.L. Mielke, S. Zhang, R. Khare, R.S. Ruoff, T. Belytschko, G.C. Schatz, The effects of extensive pitting on the mechanical properties of carbon nanotubes, Chem. Phys. Lett. 446 (2007) 128–132.

[35] L. Pan, Z. Shen, Y. Jia, X. Dai, First-principles study of electronic and elastic properties of Stone–Wales defective zigzag carbon nanotubes, Phys. B: Condens. Matter 407 (2012) 2763–2767.

[36] R. Khare, S.L. Mielke, J.T. Paci, S. Zhang, R. Ballarini, G.C. Schatz, T. Belytschko, Coupled quantum mechanical/molecular mechanical modeling of the fracture of defective carbon nanotubes and graphene sheets, Phys. Rev. B 75 (2007) 075412.

[37] R.H. Poelma, H. Sadeghian, S. Koh, G.Q. Zhang, Effects of single vacancy defect position on the stability of carbon nanotubes, Microelectron. Reliab. 52 (2012) 1279–1284.

[38] N.M. Pugno, J.A. Elliott, Buckling of peapods, fullerenes and nanotubes, Phys. E: Low-Dimens. Syst. Nanostruct. 44 (2012) 944–948.

[39] Y. Kuang, S.Q. Shi, P.K. Chan, C.Y. Chen, The effect of intertube van der Waals interaction on the stability of pristine and functionalized carbon nanotubes under compression, Nanotechnology 21 (2010) 6.

[40] H. Song, X. Zha, Molecular dynamics study of effects of sp3 interwall bridging and initial vacancy-related defects on mechanical properties of double-walled carbon nanotube, Phys. B: Condens. Matter 403 (2008) 3798–3802.

[41] Z. Qin, Q.-H. Qin, X.-Q. Feng, Mechanical property of carbon nanotubes with intramolecular junctions: molecular dynamics simulations, Phys. Lett. A 372 (2008) 6661–6666.

[42] X. Hao, H. Qiang, Y. Xiaohu, Buckling of defective single-walled and double-walled carbon nanotubes under axial compression by molecular dynamics simulation, Compos. Sci. Technol. 68 (2008) 1809–1814.

[43] N. Hu, K. Nunoya, D. Pan, T. Okabe, H. Fukunaga, Prediction of buckling characteristics of carbon nanotubes, Int. J. Solids Struct. 44 (2007) 6535–6550.

[44] N. Chandra, S. Namilae, Tensile and compressive behavior of carbon nanotubes: effect of functionalization and topological defects, Mech. Adv. Mater. Struct. 13 (2006) 115–127.

[45] V.P. Nguyen, M. Stroeven, L.J. Sluys, Multiscale failure modeling of concrete: micromechanical modeling, discontinuous homogenization and parallel computations, Comput. Methods Appl. Mech. Eng. 201–204 (2012) 139–156.

[46] S. Bishnoi, K.L. Scrivener, μic: a new platform for modelling the hydration of cements, Cem. Concr. Res. 39 (2009) 266–274.

[47] J.M. Wernik, S.A. Meguid, Multiscale modeling of the nonlinear response of nano-reinforced polymers, Acta Mech. 217 (2011) 1–16.

[48] M. Kulkarni, D. Carnahan, K. Kulkarni, D. Qian, J.L. Abot, Elastic response of a carbon nanotube fiber reinforced polymeric composite: a numerical and experimental study, Compos. Part B: Eng. 41 (2010) 414–421.

[49] K.I. Tserpes, P. Papanikos, G. Labeas, S.G. Pantelakis, Multi-scale modeling of tensile behavior of carbon nanotube-reinforced composites, Theor. Appl. Fract. Mech. 49 (2008) 51–60.

[50] M. Matsumoto, T. Nishimura, Mersenne twister: a 623-dimensionally equidistributed uniform pseudo-random number generator, ACM Trans. Model. Comput. Simul. 8 (1998) 3–30.

[51] B. Patzák, D. Rypl, Object-oriented, parallel finite element framework with dynamic load balancing, Adv. Eng. Softw. 47 (2012) 35–50.

[52] S. Mohammadi, Extended Finite Element Method: for Fracture Analysis of Structures, 2008.

[53] S. Mohammadi, XFEM Fracture Analysis of Composites, Wiley, 2012.

[54] M. Jirásek, M. Bauer, Numerical aspects of the crack band approach, Comput. Struct. 110–111 (2012) 60–78.

[55] D.A. Hordijk, Local approach to fatigue of concrete, in: Civil Engineering and Geosciences, Delft University of Technology, 1991.